Progress Report 2013 and Beam Request for 2014

Muon Capture on the Deuteron

The MuSun Experiment

PSI Experiment R-08-01, spokespersons P. Kammel, C. Petitjean, A.A. Vasilyev

MuSun Collaboration [1]

Petersburg Nuclear Physics Institute – University of Washington (Seattle) – Paul Scherrer Institut – University of Kentucky – Boston University – Regis University – University of South Carolina

http://muon.npl.washington.edu/exp/MuSun

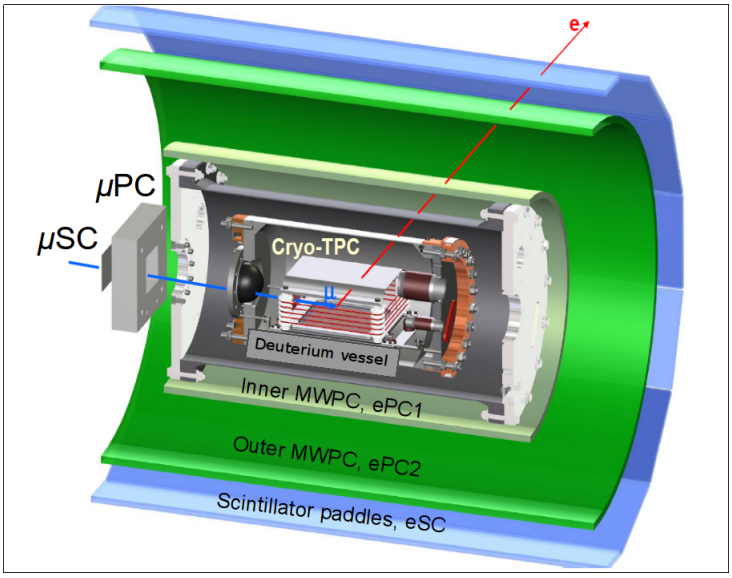

Figure 1: MuSun detector model. Muons pass through entrance detectors to stop in a deuterium target TPC. The decay electron is detected in two cylindrical wire chambers (green) and a 16-fold segmented scintillator array.

Contents

1 Introduction

In 2013 we published the final result of the MuCap experiment [2], which is a precision determination of g_P, the weak-pseudoscalar coupling of the proton. The hydrogen time projection chamber (TPC) technique employed is relatively immune to the poorly known molecular physics complications that plagued previous efforts. The result, $g_P = 8.06 \pm 0.55$, settles a long-standing experimental challenge. It provides a sensitive test of QCD symmetries and finally confirms a fundamental prediction of chiral perturbation theory. The result was recognized as an Editor's Suggestion and described in an American Physical Society synopsis and in several press releases.

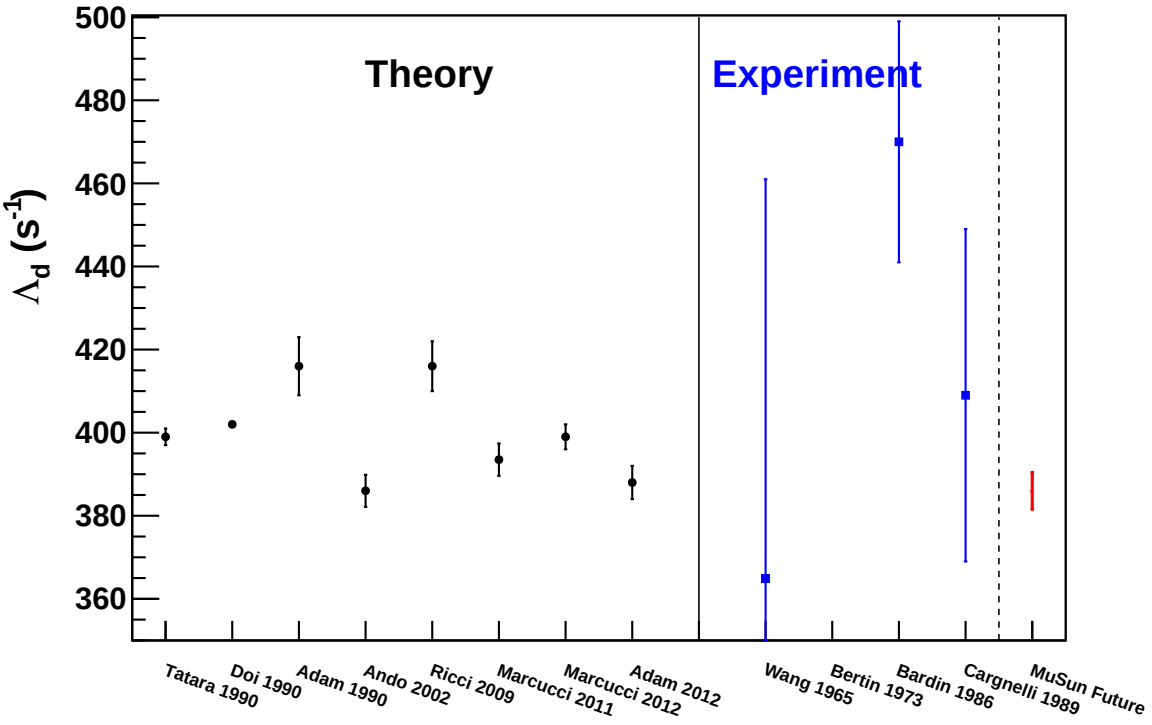

Figure 2: Recent theoretical and experimental results on muon capture rate Λ_d from the doublet state of the μd atom. The pion-less EFT calculation [3] cannot be readily expressed by a single value and is not included. Bertin 1973 is off scale (c.f. [4]). Experimental results scatter widely and the most accurate result is inconsistent with modern theory. The ambitious precision goal of MuSun is indicated.

The good agreement between the MuCap result and theory demonstrates that all parameters entering the *one-nucleon* weak amplitudes are well under control. This allows the MuSun experiment to extend this program with a precise determination of the strength of the weak interaction in the *two-nucleon* system, using the process

$$\mu + d \to n + n + \nu. \tag{1}$$

MuSun will determine the sole unknown low-energy constant involved in modern – QCD-based – effective field theory (EFT) calculations of weak nuclear reactions. The anticipated precision is 5 times greater than presently available from the 2N system and will be essential for calibrating these reactions in a model-independent way. This will provide a benchmark for extending the EFT method to more complicated few-body processes. Regarding the 2N system, muon capture will provide unique constraints on electro-

weak astrophysical processes of fundamental importance, whose rates have never been measured directly. These include *pp* fusion, which is the primary energy source in the sun and the main sequence stars, and the νd reaction, which provided convincing evidence for solar neutrino oscillations at the Sudbury Neutrino Observatory. The recent status and tension between experiment and theory on muon capture on deuterium is depicted in Figure 2, updated from last year's Progress Report.

MuSun measures Λ_d, the capture rate from the doublet hyperfine state of the muonic deuterium atom in its 1S ground state, by determining the negative muon lifetime τ_- in a time projection chamber filled with ultra-pure deuterium gas at cryogenic temperatures. The capture rate is derived from the difference $\Lambda_d \approx 1/\tau_- - 1/\tau_+$, where τ_+ is the positive muon lifetime [5]. As sketched in Fig. 1, the detector consists of muon detectors (muSC, muSCA, TPC), electron detectors (ePC1/2, eSC) and neutron detectors (not shown). For a more detailed discussion of the novel experimental strategy, we refer to our earlier Reports. The physics aspects of this field are covered in review [4].

In this Report we will present the ongoing analysis of our first production run in 2011 (R2011), the overview of our first production run (R2013) in the new πE1 area and conclude with our plans for this year and the beam time request. The 2014 run will provide theses material for several Ph.D. students, continuing our strong commitment to training and research (In 2013 four undergraduate and seven graduate students participated in MuSun at PSI).

2 Status of the Analysis of Run R2011

2.1 Analysis Framework for Lifetime Analysis

The analysis framework for MuSun data is based heavily in C++, using ROOT and the modular MIDAS software developed at PSI. Analysis proceeds in multiple stages, with each stage processing increasingly high-level physical objects. In the first stage, raw information from detectors is translated into objects with physical significance, such as electron or muon tracks. Additionally, low-level checks on detector performance and calibration are performed. In the second stage, these physical objects are correlated in order to produce the decay time distributions that are fitted to extract the muon lifetime. High-level systematic checks are also performed in the second stage. The MuSun analysis is performed with the absolute clock frequency blinded, and additional blinding between positive and negative muon data is implemented in software.

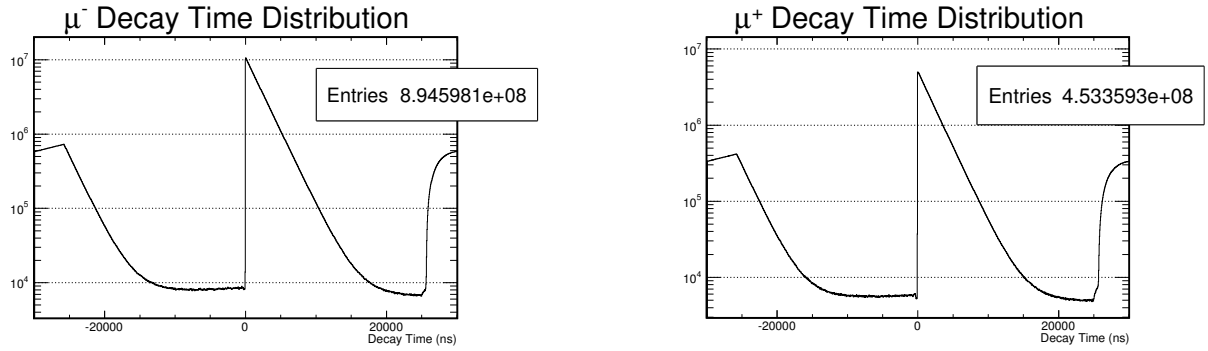

Figure 3: Left: μ^- decay time distribution, about 20% of the R2011 dataset. Right: μ^+ decay time distribution, full R2013 dataset.

The computational requirements for MuSun preclude doing the analysis using solely locally available computers, so an allocation of 200,000 SU (cpu-hours) is maintained on the Lonestar cluster at the Texas Advanced Computing Center. This allocation was recently renewed for the calendar year 2014 and includes another allocation of 210 TB of mass tape storage on the Ranch archive.

Crucial to the extraction of the muon lifetime is a robust muon track finder that is insensitive to systematic distortions of the decay time distribution by physical and algorithmic effects. The primary function of the track finder is identifying muons that stop in the fiducial volume of the TPC gas, while rejecting muons that leave this volume. Additionally, the three-dimensional position and timing of muon and other charged particle tracks in the TPC are used for secondary systematic studies. The efficiency for accepting muon stops must not be coupled to the decay time of the muon.

2.2 Systematic Effects

The primary reaction for stopped muons in MuSun is decay to a Michel electron ($\mu \rightarrow e + \nu + \bar{\nu}$). A known systematic distortion of the measured muon lifetime is due to the interference of an electron track with the acceptance of muon stops. The electron is nearly invisible in the TPC, but the small amount of energy deposited in the stopping pad can push a muon track over the acceptance threshold. Events with early decay times, where the electron track most overlaps the drifting cloud of ionized electrons from the muon track, are more likely to be accepted.

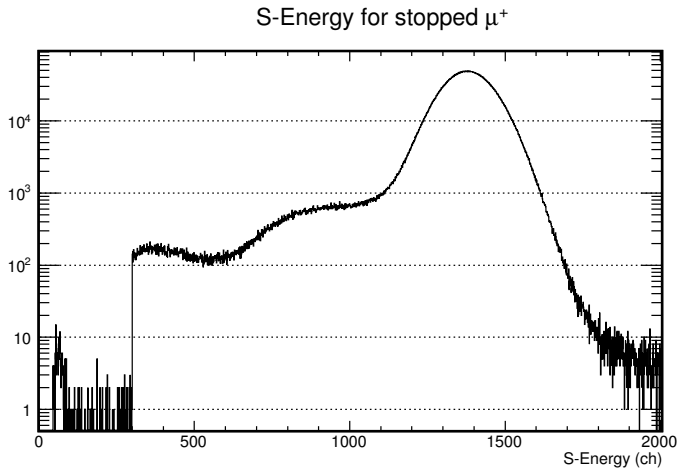

Figure 4: Distribution of muon S-energy. The nominal cut is at 300 channels. The low-energy shoulder is composed partly of high-angle scattering events and partly of decay-in-flight muons.

To study this effect, we can use stopped μ^+, since the Michel decay mode is nearly identical, but the positive muons do not undergo capture or muon-catalyzed fusion as with μ^-. Electron interference is highly geometry-dependent - at early decay times, the strongest effect is due to horizontal electron tracks but downward-going tracks have the largest effect at late times. The change in the fitted lifetime as a function of azimuthal angle of the decay electron track provides a way to quantify the interference effect. In addition to the electron track direction, we can enhance the interference by varying the cut on the muon stop energy. To this end, we introduce a quantity called the S-energy, equal to the sum of the stopping pad energy and twice the next-to-last pad energy (the TPC readout plane is segmented into 48 pads). The S-energy is a well-peaked value (Figure 4), independent of where in the pad the muon stops. The electron interference should be largest when the population of muons that could be pushed over the threshold is largest - that is, at the peak of the S-energy distribution. An S-energy threshold of 1300 channels enhances the electron interference dramatically (Figure 5). However, at the nominal energy cut of 300 channels, there is no dependence of the fitted muon lifetime on the azimuthal angle of the electron track, indicating that MuSun can avoid this systematic effect by choosing a low enough muon energy threshold.

The next most common reaction that stopped muons undergo in MuSun is muon-catalyzed fusion (MCF), via the reactions $\mu^- d \rightarrow \mu^- + {}^3\mathrm{He} + n$ and $\mu^- d \rightarrow \mu^- + t + p$. Fusion interference is the

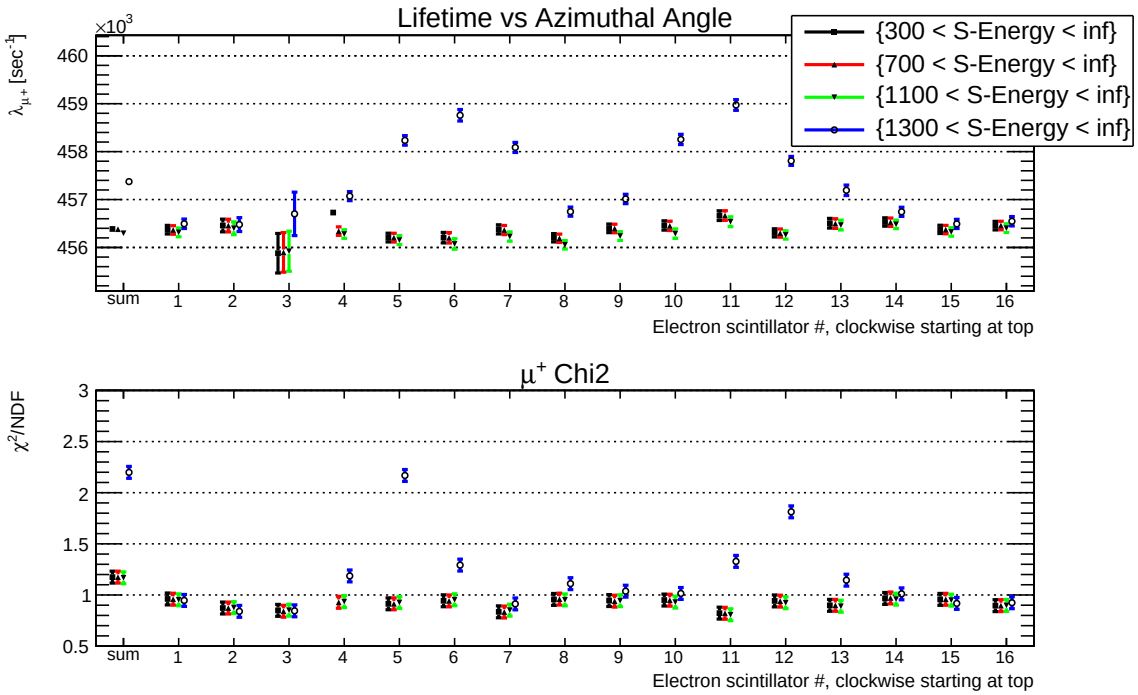

Figure 5: Measured muon disappearance rate as a function of azimuthal section of the electron detector. Color indicates varying cut on the muon S-energy. At the nominal cut of 300 energy channels, there is no trend, but cutting in the middle of the S-energy distribution shows a large electron interference effect, strongest in the horizontal directions. The disappearance rate is blinded, both absolutely and with respect to the negative muon disappearance rate.

coupling of the acceptance of a muon stop to the detection of the charged fusion products in the TPC. Misconstruction of the muon energy leads to an effect similar to electron interference, though in this case later decay times are enhanced. On the other hand, misconstruction of the muon stop position due to the longer proton track can accept or reject muon tracks with the fiducial volume cut. For example, using a naive muon track finder, we can fit the muon lifetime for slices of the TPC in a direction transverse to the beam (Figure 6). The difference between μ^+ and μ^- is attributed to fusion interference.

In order to calibrate the sensitivity of a muon track finder to the presence of MCF fusion products, we must be able to change the magnitude of fusion interference. In the data, the effect of misconstruction of the muon stop energy on the muon lifetime can be studied by varying the muon stop energy threshold, as with electron interference. Misconstruction of the muon stop position has an effect at the boundaries of the fiducial volume, so varying the size of the fiducial volume changes the relative contribution of this interference to the decay time distribution. Additionally, the gradient of the muon stop spatial distribution will determine to what extent the effect of erroneous muon stop rejections and acceptances balance each other out. To address both versions of fusion interference, simulations of fusion tracks and the systematic distortion to the muon lifetime are ongoing. Another effort is an alternative muon track finder based only on the energy deposition far upstream from the stopping point. The finite range of the fusion products prevents a correlation between fusion products and the acceptance of muon tracks.

A population of muons stopping in materials other than deuterium will undergo nuclear capture with a different rate, distorting the decay time distribution. The muon track finder must not misidentify stops such that a muon stopping in wall materials is accepted. Analysis of the R2011 data indicated that it is possible for muons to scatter at high angles from D_2 nuclei and travel invisibly in the TPC drift direction, stopping in the anode or cathode of the TPC (Figure 4). This motivated the construction of TPC components from very high-Z materials for R2013. In very high-Z materials, capture occurs before

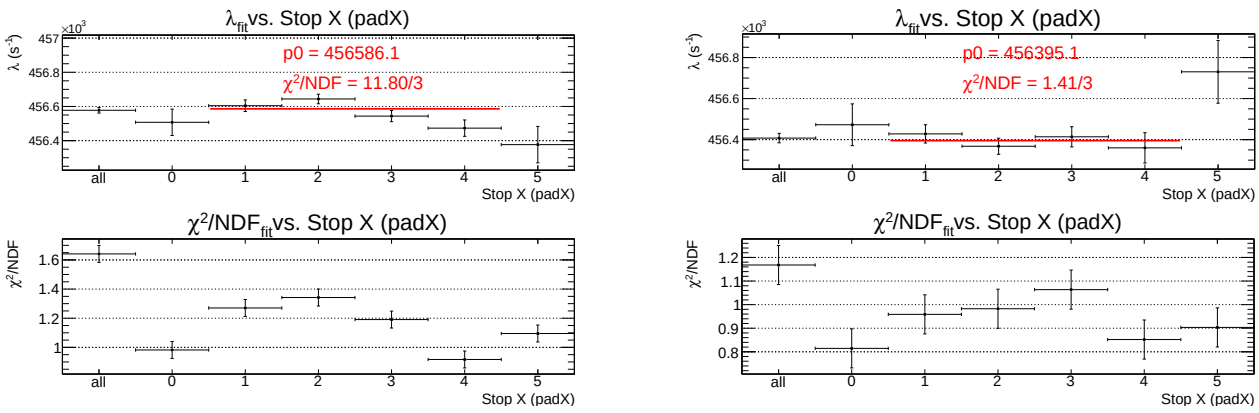

Figure 6: Left: μ^-, Right: μ^+. Measured muon disappearance rate as a function of stopping coordinate transverse to the beam direction and TPC drift field. The μ^+ and μ^- disappearance rates are blinded, both absolutely and with respect to the negative muon disappearance rate. The red bar shows the fit to a constant over the fiducial volume.

the start time of the fit to the distribution, so no distortion is measured. The R2013 anode pads are silver, the Frisch grid and wires are tungsten, and the cathode is a silver foil. These high-angle muon scatters will be studied further, both for the analysis of R2011 data and to quantify the contribution in R2013. The detection of neutrons ejected from nuclear muon capture provides an additional indirect measure of how many muons stop in materials other than deuterium.

Chemical impurities in the deuterium distort the decay time distribution as muons transfer preferentially to the impurities and capture with a rate different than on deuterium. Careful analysis of signals following the muon stop in the R2011 TPC showed that the recoiling nucleus from this muon capture can be detected, though the muon-catalyzed fusion is a large background. Because these events can be used to measure the chemical purity of the target gas *in situ*, this motivated a major effort to improve the TPC energy resolution and build an array of X-ray detectors to tag the transfer to a nitrogen or oxygen nucleus (Section 3.6.2). In R2011, the uncertainty in the chemical purity of the gas will contribute a significant uncertainty to the final error. There are avenues for improvement however, such as reducing the backgrounds from noise pulses via a shape analysis of the waveforms.

An anomalous correlation between the muon entrance time and the time of the electron track was discovered in the R2011 data. This fluctuation is most visible in the fit residuals from the decay time distribution and disappears after the first microsecond (Figure 7) The fluctuation is present in both μ^+ and μ^- data and exists when only the entrance detectors and the electron scintillator are included in the analysis. The effect does not appear to be present in the R2013 data at the same magnitude, though further, higher-statistics analysis will determine if it is completely absent.

As a similar fluctuation was observed in the baseline of the electron tracking scintillators. A time spectrum of the deviations from the average pedestal vs. time for one particular channel is shown in Figure 8. In the context of the analog signals, the oscillations obtained from the digitized waveform are not terribly large, no more than 0.4 mV in amplitude. However, their effect on the lifetime spectra is enhanced by the fact that the eSC trigger threshold is set, out of necessity, in a place where there is a great amount of data, as is clear from Figure 9. There simply is no clear separation between the noise and the Landau peak.

Since MuSun has long since moved out of $\pi E3$, it is unlikely that we will ever understand the origin of the oscillations in the eSC pedestals. No sign of them was seen in the two years of running with the MuCap experiment. And like the fluctuations in the fit residuals, they have not returned in the R2013 data Figure 8. In order to correct for this issue, our first approach has been to employ a time-dependent

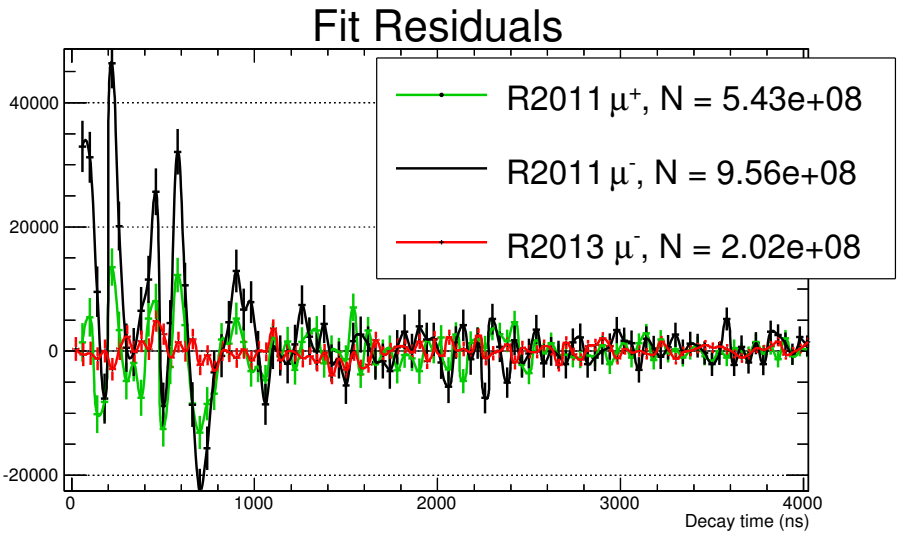

Figure 7: An anomalous correlation between the muon entrance time and the time of the electron track appears in both μ^+ and μ^- for R2011, but the effect is much smaller in R2013.

software cut on the maximum sample in the waveform. Since we need to make corrections no larger than 0.4 mV, the maximum sample in the waveform does not have enough digital resolution (our 8-bit waveform digitizers have a resolution of ∼4 mV). Therefore, we smear this maximum value by $\pm\frac{1}{2}$ ADC counts so as to create a continuous distribution. We can now make time-dependent software cuts on the individual triggers using time-dependent correction functions derived from the corresponding pedestal oscillations. We are hopeful that this pedestal correction (now being tested in a pilot production run) will remove the early time oscillations in the fit residuals. If successful, this correction would underscore the necessity of storing the full waveform record compared to the simple discriminator/TDC information.

2.3 Monte-Carlo Simulations

The MuSun Monte Carlo is based on the most recent release of GEANT4, which has important improvements in the handling of low energy electromagnetic processes. Information about particles passing through sensitive detectors (the muon entrance counters muSC and muPC, the TPC and the electron detectors ePC and eSC) are stored in a root file for later processing. We also store the interesting GEANT tracks so we can do a detailed comparison of reconstructed events with the so-called GEANT "truth." The run dependent parameters, such as deuterium pressure and temperature as well as beam properties, are initialized via a GEANT macro. This not only enables us to simulate different configurations, such as R2011 and R2013, without recompiling the code but by including a copy of this macro in the root file we are able to document the simulation conditions as well as pass on information needed by the detector response package.

The detector response package reads the root file created by GEANT and produces a MIDAS file which has the same format as the raw data collected by the experiment. For the experimental data, a number of parameters such as timing offsets, coincidence windows, thresholds, gains and pedestals, are stored in an online database which is used in the first analysis stage (event reconstruction). In the Monte Carlo response program we use this same database when simulating events so as to enable the processing of different run conditions without any modifications.

A number of improvements have been made in the simulation of the detector response over the last year. A noise model of $1/f^\alpha$ has been tuned using forced trigger data for both R2011 and R2013. A detailed comparison of S-energy, energy deposited on the stop pad and cluster widths shows that some aspects are sensitive to electronic noise but some are sensitive to drift, and it was realized that the effects

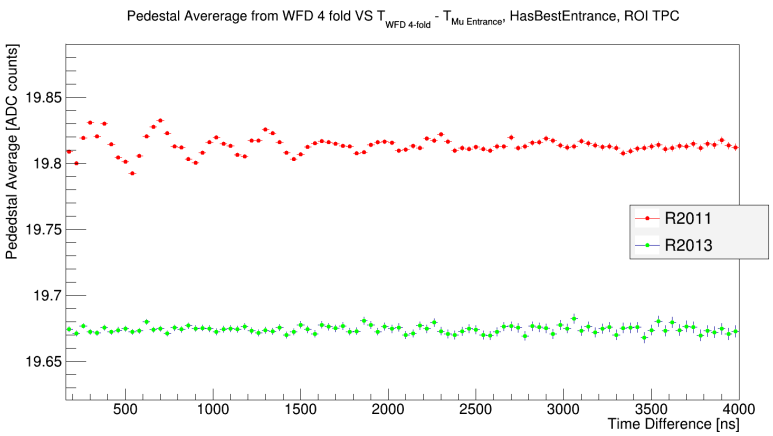

Figure 8: Time correlations between the eSC pedestals and muon disappearance time for R2011 and R2013

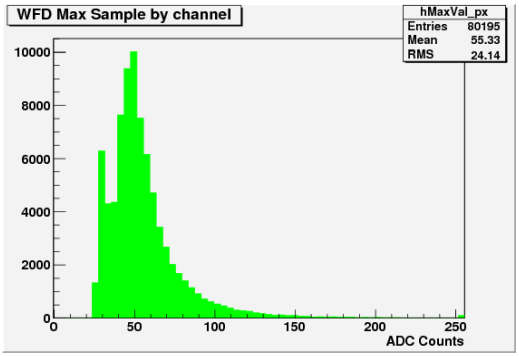

Figure 9: Spectrum of maximum samples for a typical eSC PMT. Note the poor separation between signal and noise.

of the Frisch grid had not been modeled correctly. It is known that heavily ionizing particles, such as ^{3}He, appear at a lower energy because some of the ionization electrons recombine with the ions before they can drift to the pad plane. This effect has been modeled using a Birks parameterization, $A = A_0/(1+k\frac{dE}{dx}/E_d)$ where E_d is the drift field. While this works reasonably well we are still exploring the dependence of k on the gas conditions (we find $k \propto P^2$).

We want to use the Monte Carlo as a tool to check how fusions affect the fiducial volume definition of μ^- stops. For this purpose the Monte Carlo stopping distribution must be similar to the data. When we use a turtle calculation of the beam transport for the μ position and angle at the muSC position we find that the Monte Carlo Y and Z stopping positions are narrower than the R2011 data. By adding 1.5 mm of plastic scintillator near the muSC position we can bring the Monte Carlo into better agreement with R2011. It will be interesting to compare R2013 where we had runs with a narrower beam momentum width also different pressures which should affect the straggling.

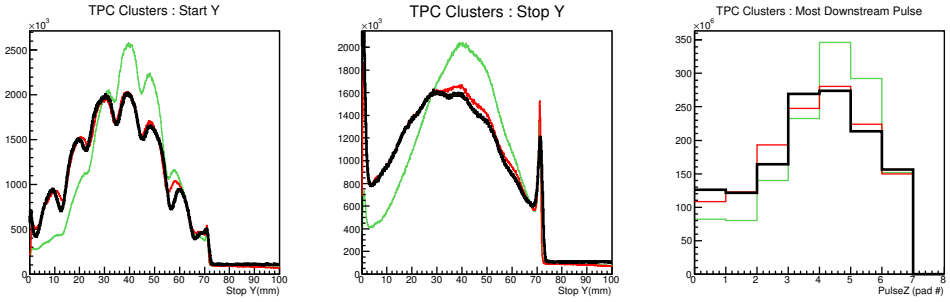

Figure 10: Y start and stop positions and Z stopping pad of clusters in the TPC. For start Y we see the shadows of the field shaping wires. A sample of R2011 data is drawn in black, the Monte Carlo with the nominal amount of material in green and the Monte Carlo with added material in red.

High-statistics simulation Each step of the simulation chain, GEANT, response and first analysis stage, takes about an hour to process 10^6 events. We have been allocated CPU time and storage on the Lonestar cluster for the purposes of generating several Monte-Carlo data sets of 10^9 reconstructed μ events. Lonestar is a DELL Linux Cluster with over 22,000 cores, optimized for running parallel jobs. We have written a set of scripts to run multiple GEANT, response and first analysis stage jobs in parallel, so by using many cores we can process of the order of 10^9 events for each step in an hour or two. These

scripts record the running conditions and results in an SQLite database for documentation. We have recently run samples of about 2×10^9 events for both μ^- and μ^+ events using R2011 conditions. While Lonestar performed well we find that about 10% of the jobs fail in both the response and first stage analysis steps because of issues relating to use of shared memory by MIDAS. Although these failures appear to be random and simply re-processing the failed jobs works, we still get "charged" for wasted CPU time. Since the issue also affects the processing of experimental data we are currently working on fixing this problem.

3 Report on Physics Run R2013

3.1 Goals

The main goals and events of our run in 2013 (R2013) were as follows:

- **Final commissioning of new πE1.2 area.** The basic installation, achieved in 2012, was finalized with the commissioning of two new quad triplets, the installation of a fully movable detector setup supported by a rail system, dynamic cable carriers, the commissioning of new gas alarm and slow control systems and the installation of a climatized tent to house the detector systems and electronics.

- **TPC upgrade.** To minimize the effect of errant muon stops, the TPC was upgraded with high-Z materials as much as possible. New components included a thick silver-coated pad plane, a tungsten grid frame, tungsten field wires, and a silver foil as the high voltage cathode. The tungsten grid frame used a new wire-mesh geometry and soldering method, which allowed the required grid field to be achieved for the first time. The new frame operated successfully for several weeks, but eventually failed during a temperature cycle.

- **TPC resolution upgrade.** The external preamplifiers were replaced by newly-designed miniature cryogenic preamplifiers working in the insulation vacuum at close proximity to the cold volume of the TPC. The additional risk of operating the preamplifiers in this challenging and hard-to-access environment was justified by nearly flawless operation and a dramatic improvement in resolution. This had to be paired with an increase of the digital resolution of the readout system (8-bit waveform-digitizers) and by operating the two systems at different dynamic ranges.

- **Optimal Run Conditions and Impurity Monitoring.** The cold head was repaired so as to achieve sub 30 K TPC temperatures once again, and the R2013 experience should determine the optimal running conditions for MuSun. The choice of temperature and density is a compromise between several factors, and it critically depends on the purification and impurity monitoring capabilities of the experiment. A highlight of R2013 was the demonstration and calibration of the much-improved sensitivity of MuSun's impurity monitors. An issue requiring scrupulous attention in future runs was an unprecedented saturation of the purification system.

- **Resolution of R2011 puzzles.** A major puzzle in the R2011 analysis was the appearance of unexpected early-time oscillations in the observed time spectra of Michel electrons after muon decay. Several hardware adjustments and systematic studies were performed to address this issue. The R2013 spectra appear to have largely eliminated these distortions, and the analysis of additional information recorded in 2013 might shed light on the earlier puzzles.

- **Production data set of close to 10^{10} events.** We were planning to collect nearly half of the required full MuSun statistics in 2013, but ended up with only about 2×10^9 events under optimal running conditions, excluding systematic studies. This loss was primarily caused by a very unusual event at PSI; an extended downtime in excess of 4 weeks caused by problems in the flat-top cavity

of the main accelerator. The accelerator problems appeared with unfortunate timing: just after the MuSun set-up period. Additional smaller losses in the data taking were related to the time required for final commissioning, TPC impurity issues, and the grid malfunction mentioned above.

3.2 Chronology

The first three beam weeks were used to prepare the detectors, front-end electronics, and data acquisition systems for the data-taking period. Major activities included final infrastructure installations in the area, beam commissioning, tuning of the cryogenic and purification systems and preparation of the new time-projection-chamber (nTPC). While the nTPC was being assembled, the old TPC from R2012 was used for beam tuning and for studying the performance of the new cryo-preamplifiers and the dependence of the energy resolution on the chamber voltages and gas pressure.

During the same period, we looked for signs of the early-time effects discovered in the R2011 data. We tested the electron detectors and muon entrance detectors under varying conditions: running with or without the kicker enabled, using the Michel electrons or ^{90}Sr source as electron signals, and using the muon beam or a 25 kHz clock as the muon entrance signal. We saw no sign of the early-time oscillation, neither in our preliminary studies nor in the production run that followed. However, during this process, we noticed some intermittent bit-dropping problems in the WFDs used to read out electron detectors, problems which seemed to migrate through the crate housing the WFDs. We solved the problem by reducing the master clock frequency from 500 MHz to 450 MHz.

Once the nTPC was assembled it replaced the old TPC. Unfortunately, a gas leak from the deuterium vessel to the insulation vacuum volume was observed: the source of the leak was either the indium seal or a deficiency of the cold multi-pin feedthrough flange. We then decided to place the central detection elements of the new system within the old pressure vessel. The new detector operated with a cathode voltage of 80 kV and a grid voltage of 3.6 kV. The 25% higher grid voltage compared to the old TPC is essential to achieve full charge collection, which produces larger TPC signals and superior energy resolution.

Renewed data taking with nTPC was inhibited by a major accelerator failure due to overheating of the flat-top cavity in the main ring, which lasted for three weeks. After that data taking resumed, starting with a few days of system tuning. The clock frequencies were then blinded from the collaboration, and production started on Oct. 16. The only significant problem we encountered in the first few days was low efficiency in the electron detector, which was corrected by increasing the voltage on the eSC phototubes. We then obtained approximately two weeks of production data with stable conditions in the TPC: cathode high voltage of 80 kV, grid high voltage of 3.6 kV, and deuterium temperature of 31 K and pressure of 5.1 bar.

Data taking was only interrupted by occasional sparks in the TPC, which would bring the data acquisition system to a halt for brief periods of time. During this time the direct impurity capture detection described in section 3.6.2 was developed at the required sensitivity level, and the results suggested an unexpectedly high impurity signal. This was further confirmed by gas chromatography. Alas, our cleaning system was not properly working, due to the saturation of the zeolites, which absorb impurities from the circulating gas. Therefore we did not achieve an anticipated N_2 impurity level of 1 ppb in the TPC, but a level closer to 20 ppb. The zeolite was regenerated during the second service shutdown and the system was warmed up and then pumped. While unacceptable for future high statistics production data-taking, the enhanced impurity level of R2013 can be corrected for with a precision commensurate with the available statistics, using the developed monitoring methods.

After a second shutdown caused by the flat-top cavity problem, which lasted for ten days, we began the systematic error measurement program. Our principle objectives were to refine our assessment of TPC impurities using gas chromatography and the capture recoil method, measure the effect of impurities on the lifetime,determine the muon transfer rate to nitrogen at the relevant cryogenic temperatures, and thus define the optimal running condition for R2014.

Just after the beam returned, the TPC signals from some pads were found to be missing or abnormal, and it was soon evident that the grid was shorted to ground. Upon opening the TPC, we found that there were broken grid wires at the upstream and downstream side, and that an edge of the cathode plane was floating loose. We used the old TPC grid and cathode to replace the broken ones, which left us only about 6 days for the systematic measurements. For these final measurements, the cathode and grid HV were set at 75 kV and 2.7 kV respectively. We first returned to the production conditions (31 K, 5.1 bar). By measuring impurities using both the capture recoil and gas chromatography methods, we confirmed that CHUPS was working properly. Then, after doping the deuterium gas with 3 ppm N_2, we took data at TPC temperatures 37 K and 34 K. Data at these two temperatures, where the N_2 concentration is fixed to the vapor pressure curve, will allow the extrapolation of impurity distortions of the muon lifetime to the impurity concentrations of our production data. Moreover, this measurement will calibrate impurity corrections for future runs. Finally, the deuterium density was reduced to 60% of the nominal value. We took data at 37 K and 28 K to test whether reduced density is a suitable option for R2014.

In conclusion, we accumulated two weeks of production data in R2013 and collected approximately 2×10^9 stops for μ^- and 2×10^8 stops for μ^+ (see Figure 11), after applying all selection cuts. The slope of the smooth data taking shows that we can obtain 10^9 per week, which means we need ten weeks of steady data taking to reach 10^{10} good muon stops.

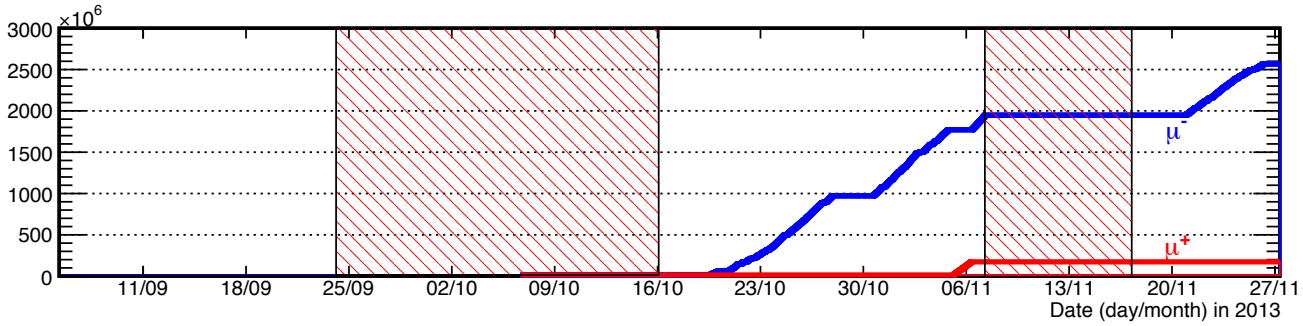

Figure 11: Accumulated statistics for R2013, counting $\mu - e$ decay pairs with a track in the TPC target fiducial volume and a well-identified electron track. The shaded regions correspond to extended downtime of the PSI high-intensity proton accelerator.

3.3 Commissioning of the Area

Area gas alarm system. In the course of the new πE1 area development, PSI installed a new stationary gas alarm system consisting of two flammable gas sensors, one dedicated H_2 sensor and three oxygen deficiency monitors. The gas sensors are now connected to the main alarm system and will trigger an emergency response by the fire brigade. The MuSun experimental team documented the proper response for the external emergency team and designed an upgraded alarm and interlock system for the MuSun apparatus. The new alarm box is based on a programmable logic controller (PLC) and integrates the gas alarms with various status indicators of the MuSun apparatus. For safe operation, the alarm box provides an interlock for the TPC high voltage and controls a series of sirens and telephone calls to alert the shift crew and experts in case of an emergency. The PLC is constantly read out by the MuSun DAQ, which allows for fast diagnostics and swift action in case of an alarm. In addition, the flexibility of the programmable logic allows the alarm system to be kept live during different modes of operation. The system had to be developed and configured by the collaboration in order to meet the tight readiness schedule for the R2013. Future expansions are possible with little or no interruption.

Climate-controlled tent. A climate-controlled tent was installed over the MuSun apparatus. It allows the TPC to be moved between measuring and service positions. The whole apparatus can be moved via

three rail-mounted platforms, and all cables connecting to the movable parts are consistently mounted on a dynamic cable duct. After a run, the experiment and tent can be retracted to the downstream back wall of the area, in order to make space for another user. This operation was exercised during the transition between MuSun and the AlCap experiment, which operated in the last beam period of 2013. Several nontrivial compromises were found to achieve important functionality within the tent construction. Without careful planning, the tent frame interferes with the cold LN_2 lines that automatically feed the cryogenic system. It also does not allow crane access to the experiment. At the moment viable solutions to all these issues have been developed, so that MuSun can be retracted enough to allow the operation of other small experiments and the building of the shielding wall for μSR operation, while allowing the relocation of MuSun to its measuring position with limited effort.

Wire chamber installation/recommissioning. MuSun's large cylindrical wire chamber (ePC2) had been repaired by the PSI detector group by replacing a broken wire. During the MuSun preparation phase in June, the concentric chambers were mounted, instrumented and tested at low voltage. This was a labor-intensive job that required several weeks. The full test had to wait for the installation of the gas alarm and tent (to maintain safety and low humidity), which occurred only a few weeks into the run. Unfortunately, the chamber could not be brought up to full voltage because of a hot sector. However, we could modify the HV voltage distribution such that most of the chamber was fully operational during the data taking. Due to the extended conditioning during the run, we observed gradual improvements ; thus, we expect the chamber to be at acceptable conditions for full production data taking in 2014. A full new set of cathode preamplifiers was designed, built, and used to replace noisy cards during commissioning and running.

Slow control. A new slow control system was installed, based on a PSI standard SCS2000 MSCB analog-to-digital converter. It reads seven temperature probes located around the area as well as two humidity sensors and five Hall probes. This system also included a new MSCB-based high voltage power divider for the eSC; in addition, signals monitoring the bubbling of chamber gas and electrical discharges in the TPC are read out by a LabJack interface. Data from each these devices is logged every few seconds to a MySQL database, and graphs are produced on demand through a Web server interface.

3.4 New πE1 Muon Beam Line

As reported to BV44, a new low-energy muon beam line was commissioned in the extended area πE1-2, replacing for MuSun the previously used πE3 beam. It still was a preliminary setup using spare quadrupoles and partly improvised supply lines. Nevertheless, we could already demonstrate in 2012 that the new system produced low energy muons in the range 25 to 45 MeV/c of excellent quality with appreciable fluxes.

In the meantime, six new short, large-aperture quadrupoles, type QSN, pole radius 12.5 cm, and mounted on rail platforms were delivered and installed during August 2013. The distance between quadrupole triplets was enlarged to extend the beam by 1 m, providing more free space in πE1-2 area for the MuSun apparatus. A manually-operated vertical slit system in the center of ASK51 improves the removal of separated electrons and kicked muons. Figure 12 shows a CAD drawing of the final beam layout in area's πE1.1/2.

In a first step the (unknown) focusing strength of the new QSN quadrupoles had to be calibrated. This was done with the 28 MeV/c surface μ^+ beam, and by varying the calculated QSN magnet currents with a calibration factor. A focusing strength of 13.04 Gauss/A was found, assuming an effective length l_{eff} = 36.6 cm. A maximum μ^+ flux of 429 kHz ($\Delta p/p$ = 1.0% FWHM, I_p = 2 mA) was measured.

In a second step, the beam momentum and sign was switched to 40 MeV/c μ^-. The beam focus was optimized at a position 12 cm downstream of the beam vacuum exit window and scanned using a small scintillation counter. The scans are shown in Figs. 13 and 14. The measured beam size is 26 mm FWHM (horizontal) x 15 mm FWHM (vertical). Horizontally, the beam is slightly asymmetric, which is probably due to the structure of the half-quadrupoles at the production target.

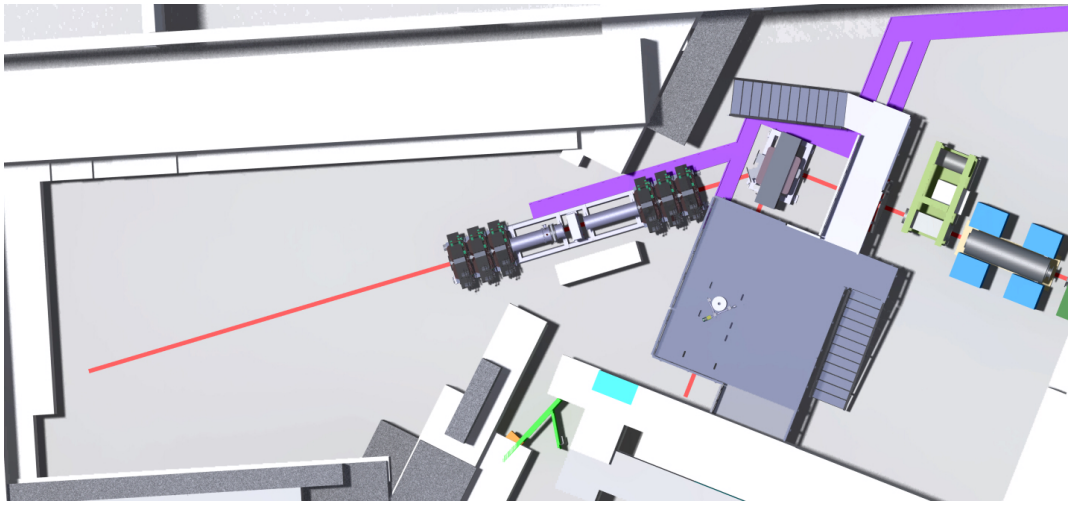

Figure 12: CAD drawing of the final πE1 low energy muon beam. The beam elements in the downstream direction are: kicker - electrostatic separator - quad doublet QSE51/52 (covered by stairs) - bending magnet ASK51 (with vertical slit in the center) - quad triplet QSN51-53 - slit system FS54 - quad triplet QSN54-56. The available free space along the beam axis is ~10 m, allowing the MuSun apparatus to roll back by up to 5 m.

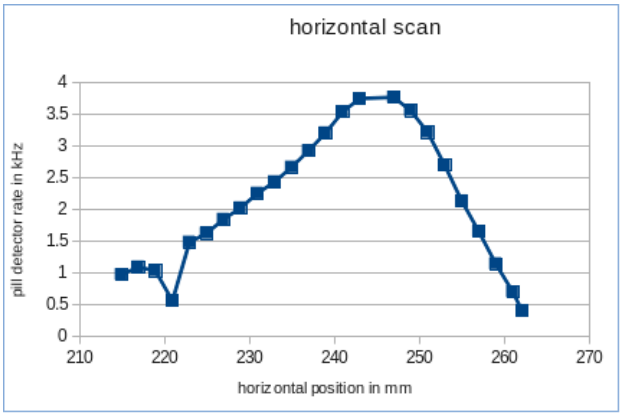

Figure 13: Horizontal scan of 40 MeV/c μ^- beam focus, x-axis in mm.

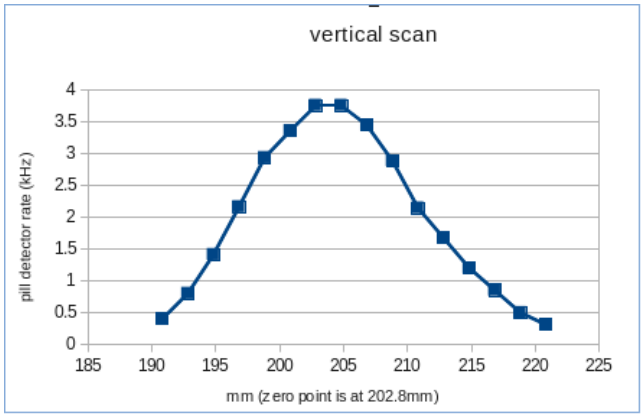

Figure 14: Vertical scan of 40 MeV/c μ^- beam focus, x-axis in mm.

Finally, our usual "beam snout" was mounted at the end of the channel vacuum tube, attached with the muSCA veto scintillator (d = 2 mm, with 35 mm beam entrance hole), the muSC trigger scintillator (d = 0.5 mm), and the muPC X-Y wire chambers (2 mm wire spacings). A typical muon stop distribution in the cryo-TPC is displayed in Figures 15. The muon stop efficiency after pileup protection and dead times was ~50%. The flux of incoming μ^- with the kicker turned on was 20 to 24 kHz (unkicked, 45 to 70 kHz), and the electron contamination with separator at 190 kV was ~10%. About 10% of the muon beam was absorbed by the muSCA counter, because it did not pass through the 35 mm hole.

3.5 System Performance

3.5.1 TPC

The TPC was upgraded for physics and technical reasons. First, it is highly preferable that muons that stop in TPC material, but are misidentified as valid D_2 stops, are captured on heavy materials. For

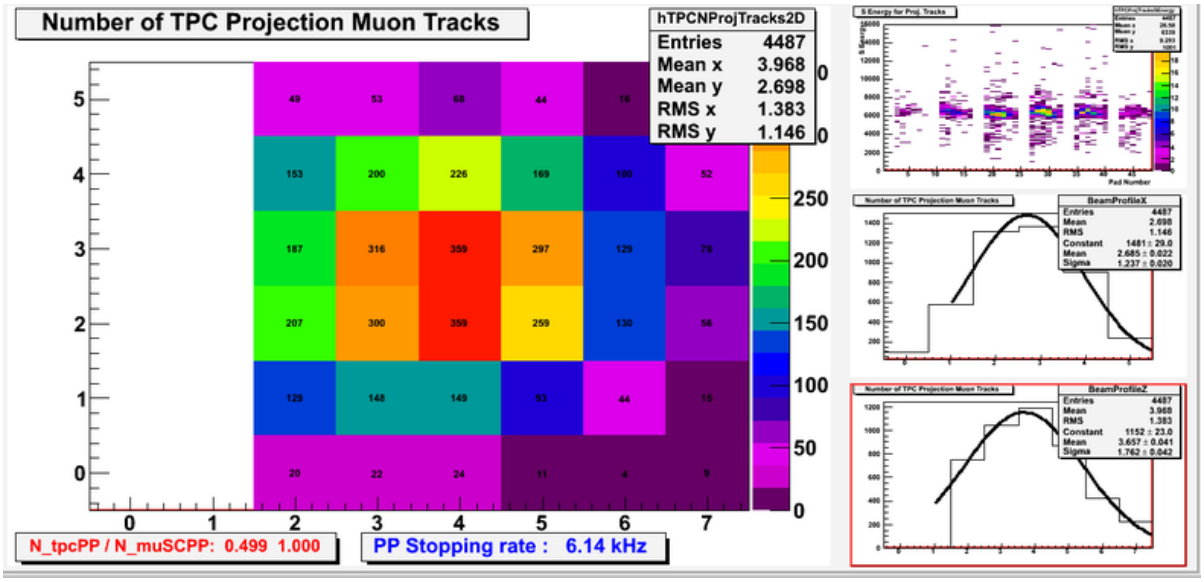

Figure 15: Typical horizontal muon stop distribution projected onto the anode pads. Beam enters from the left. The first two columns serve to define the incoming muons.

example, the μ^- lifetime in iron is 206 ns, while it is only 78 ns in tungsten. Thus it is much easier to suppress contributions from tungsten capture by a delayed time cut compared to iron contributions. Therefore, the new TPC design uses high Z material as much as possible. This was particularly challenging for the Frisch grid, as standard gold plated tungsten wires cannot be soldered to a tungsten frame. Secondly, the original TPC grid construction with stainless steel wires and frame did not reliably reach its nominal voltage for full charge collection, and it deteriorated during temperature cycles. Sparking occurred at a relatively low voltage, which is dangerous as grid sparks will likely discharge onto the pad plane and damage the sensitive input FETs of the cryogenic preamplifiers.

configuration	Φ (μm)	*pitch* (μm)	V_g (kV)	σ
old	30	250	3.3	0.028
new	50	400	3.5	0.042

Table 1: Parameters of old and new Frisch grid: wire diameter Φ, wire distance *pitch*, required grid voltage V_g, and transparency σ.

Thus a new TPC was constructed using a) a pad plane with 40 μm of silver coating on hot-fired alumina, b) tungsten field wires, c) a high voltage cathode with a 100 μm thick silver foil glued to an aluminum frame and d) a tungsten grid frame. The main concern with all of the materials is the differential thermal expansion during the cycle to cryogenic temperatures. In particular, the Frisch grid has to keep the wire tensioned at low temperatures and maintain sufficient peeling strength during the cycle.

A novel grid frame was machined from tungsten and plated with a thin layer of silver. Gold-plated tungsten-rhenium wires, tensioned by 120 g masses, were carefully soldered to the frame by the PSI detector group. A difference from the procedure used for the old frame was that the solder was applied to a planar frame surface, not to a wire winding rod. A comparison between the old and new grid geometry is given in table 1. The TPC properties [6] are determined by the grid-to-pad distance d=1.4 mm, the grid wire diameter Φ, and the distance between grid wires *pitch*. The critical parameters are the grid transparency σ, which should be small to suppress position dependence of the signal amplitude, and the grid voltage V_g, required for full charge collection given the nominal field E_d=1.1 kV/mm in the drift volume of the TPC. The old and new designs are shown in Figure 16.

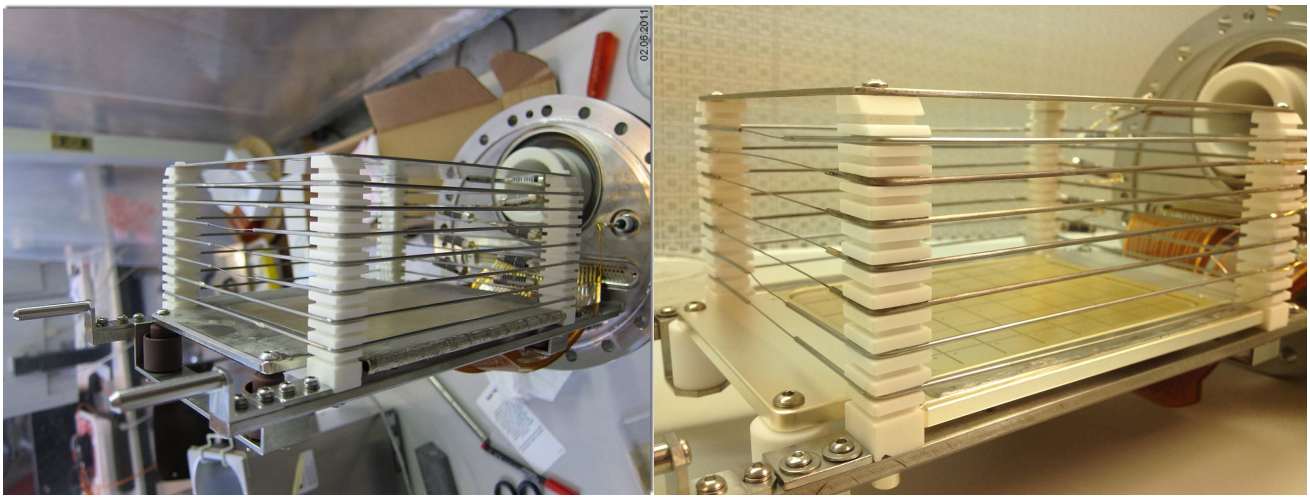

Figure 16: Left: Old TPC with grid wires strung over cylindrical support rods on stainless steel frame. Right: New TPC with planar soldering area on silver-coated tungsten frame.

The new grid performed well in terms of signal amplitude and, in particular, high voltage. Grid voltages of 3.6 to 3.7 kV could be maintained for several weeks with minimal sparking, and not a single preamplifier was damaged. Alas, the new grid mechanically failed during a temperature cycle towards the end of the run that was needed to heat and pump the TPC vessel. Some part of the solder/silver layer peeled off from the tungsten due to the differential thermal expansion between the materials. Thus, a pure tungsten construction proved not reliable enough for a long production run, and a new grid, based on a tungsten/stainless steel composite, will be constructed as detailed in Section 4.1.

3.5.2 TPC Readout

Cryo Preamplifiers

A poorly understood resolution in run R2011 first motivated an effort to improve the TPC electronics chain. In R2012, four prototype charge-integrating preamplifiers were installed inside the insulating volume adjacent to the TPC. This new location allowed for shorter input cables, which reduced the input capacitance and allowed for the unshielded kapton cables to be replaced by coaxial cables. In addition, the prototype preamplifiers were cooled to 260 K. The reduced input capacitance and cooling reduced voltage noise, while the use of shielded cables inhibited a previously-seen acoustic pickup from the residual cathode field.

In R2013 all 48 preamplifiers were replaced by the upgraded prototypes. Six modules, each containing 8 preamplifier channels were installed within the insulating volume, ∼15 cm from the cold TPC flange, as shown in Figure 18. A significant effort was made by the electronics team at the University of Washington and Regis University to compact the preamplifier circuitry, such that all channels could be mounted within the limited space. Replacement of all kapton cables, shown in Figure 17, with short insulating cables eliminated all acoustic pickup from the cathode seen previously. The resolution could be further improved by replacing the BAV99 input protection diode with a BAV199, which contributes a lower leakage current.

A new cooling system was installed, in which a vented stream of liquid nitrogen is conducted through copper tubing to a cooling block on which all aluminum preamplifier boxes are mounted. This system is capable of holding the preamplifiers at the optimal temperature of 140 K. In R2012 the RMS resolutions of the previous electronics chain were found to be 29 keV for the electronic resolution and 40 keV for the resolution of the delayed ^{3}He fusion spectrum. With all upgrades implemented in R2013, an electronic resolution below 10 keV and a ^{3}He resolution of 17 keV was achieved. A plot of the amplitude distributions

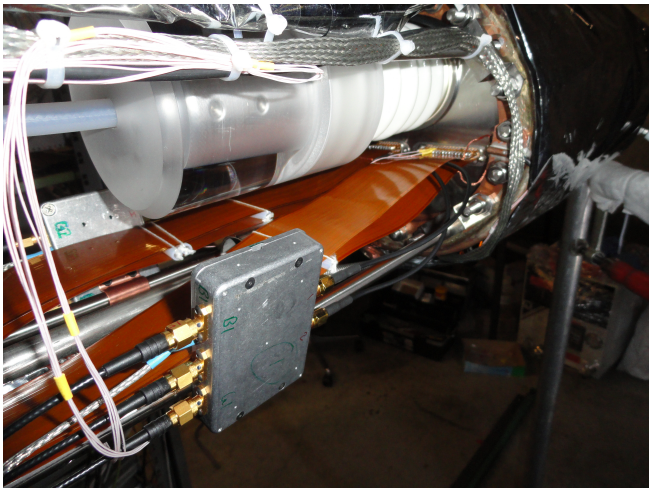

Figure 17: Previously used kapton cables, which ran from the TPC flange along the insulating volume and out to the R2011 preamplifiers, plus the mounted 2012 prototype preamplifiers. The unshielded wires picked RF and acoustic noise from the cathode fringe field.

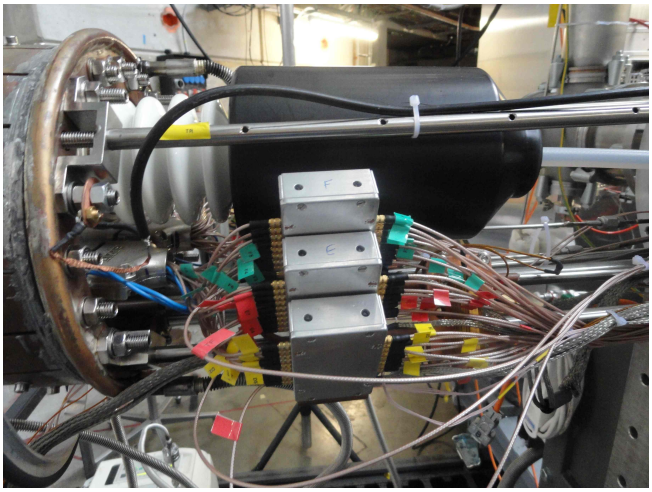

Figure 18: Symmetric mounting of the six modules each containing eight preamplifier channels within the insulating volume. Three modules are mounted on either side of the HV feedthrough on copper heat exchanger blocks which cool the preamps to 140 K.

from an injected pulse over the last three years, normalized to be the same height and centered at zero for ease of comparison, can be seen in Figure 19. This greatly improved resolution will lead to a better muon stop definition and detection of gas impurities, discussed further in Section 3.6.

Two-gain readout

To fully benefit from the remarkable resolution of the TPC, a second VME crate with 12 more TPC WFD modules from Boston University was installed. The guiding principle is that the high gain data is useful for most physics processes except the largest amplitude signals (proton signals for example), which extend beyond the range of the high gain WFDs. Instead, the largest amplitude signals are best examined with the low gain WFDs (high and low gain refer to the amplifiers, not to the WFDs, which are identical in the two crates). The two-gain system, which was installed in June of this year, worked well in the production run, with all channels operational. Some analysis challenges remain however, particularly in complicated fusion events, where a combination of high gain and low gain pulses must be integrated.

3.5.3 Electron Detector

The electron scintillator hodoscope has 16 azimuthal positions around a cylinder, each with two layers of $90 \times 15 \times 0.5$ cm^3 BC-404 scintillator that are read out from both the upstream and downstream ends. The observed signal-to-noise ratio from these detectors in previous runs was low: the waveforms were not consistent in shape from pulse to pulse, as if there were a very small number of photoelectrons or excessive pickup of interference in the cabling and electronics. We believed that these artifacts may have contributed to the dependence of the fit result on the start time that was seen in the R2011 data.

There are a total of 64 photomultiplier tubes, each with an acrylic lightguide containing several optical glue joints. One proposed explanation for the observed performance was that many of these glue joints could have been broken, reducing the light transmission. We undertook a major effort to measure this transmission. Each scintillator element was first inspected visually by placing a white light source at one end and taking a photograph of the other. A few anomalies were found during this process: for example, several photomultipliers had an air gap in place of a silicone optical coupler to the lightguide. Next, a

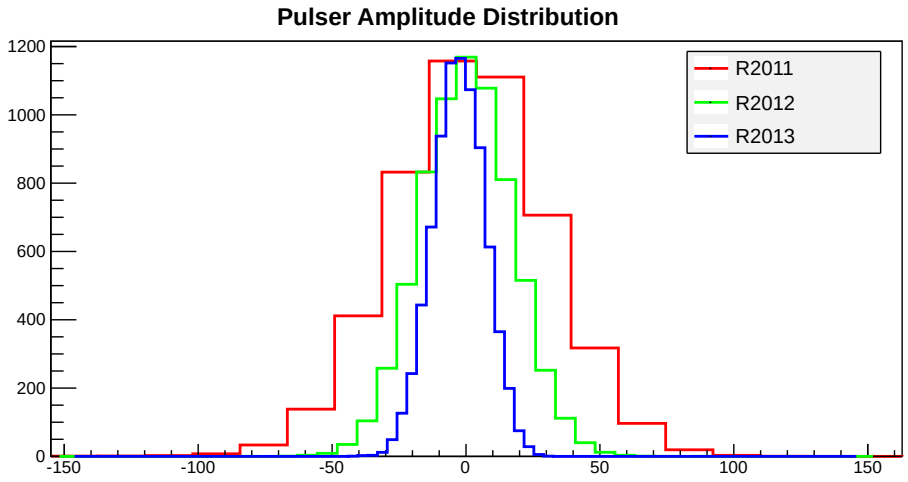

Figure 19: Amplitude distributions from an injected step pulse of charge over the last three years. The distributions have been normalized and centered at zero for easy comparison. The sigma of each distribution, in keV, shows the improving electronics resolution.

pulsed blue LED was placed at one end while a standard photomultiplier detected its light at the other. The uniformity of the transmission from one scintillator element to another appears to be at the level of ∼10%. The analysis of this measurement was complicated by a systematic drift in the output level of the LED pulser. However, we were able to take advantage of the varying pulse size in a binomial fit to estimate the number of photoelectrons from a minimum-ionizing pulse as 50.

We therefore concluded that the primary problem with the eSC was electronic, not optical. We removed attenuating resistors in the frontend circuits of the waveform digitizers, effectively doubling the gain. We also resolved some data acquisition problems related to the eSC by reducing the WFD sampling rate from 500 MHz to 450 MHz. As a test, we also set up one azimuthal position with an active split through a fanout module rather than a passive split that halves the pulse amplitude; the effective gain of these elements was multiplied by 4 compared to previous runs. We have prepared a preliminary design for an appropriate active split module that we could deploy on 64 channels if analysis shows that it is useful. The analysis of the level of improvement that we have achieved is still a work in progress.

3.5.4 CHUPS and Chromatography

CHUPS consists of two main elements: a compressor that provides a continuous flux of deuterium through the cryogenic TPC, and a block of absorbers at liquid nitrogen temperature for extraction of all air components from the deuterium. One of the main improvements of 2013 was the installation of an automatic liquid nitrogen supply system. The liquid nitrogen is used for: the compressors and the zeolite absorbers of the CHUPS system, and the cryogenic preamplifiers. For the compressors and absorbers, in previous runs we used periodically filled intermediate volumes which we had to fill every 5 or 6 hours from a liquid nitrogen tank. In 2013, an automatic liquid nitrogen supply connected to the common PSI supply system was produced and installed.

CHUPS and the cryogenic TPC were connected to the chromatograph by two direct lines (8 m tubes) for gas analyses. We have possibilities to take samples from the CHUPS output (to be sure that we produce pure gas), directly from the cryogenic TPC, and from the gas flux after TPC (before CHUPS). Direct lines with the possibility of flushing allow samples to be taken from different points of the system for comparison.

Calibration of the chromatograph was done in two ways: by air dilution, and from the nitrogen

saturation pressure at low temperatures. The air dilution method demonstrated a level of sensitivity of about 1 ppb (for nitrogen). Attempts to estimate the sensitivity level and to make an absolute calibration of the chromatographic method by the nitrogen saturation pressure at 28 to 33 K did not give stable results because we had problems with temperature stabilization. These measurements will be repeated during the technical run in Spring 2014.

In 2013, a new portion of isotopically pure deuterium was produced. For it we used the cryogenic separator developed for MuCap experiment, where we produced ultra-pure protium with a deuterium contamination less than 5 ppb. We used it to enrich commercially available deuterium from an isotopic purity level of about 0.1% to 70 ppb, which we determined from the enriched protium remaining at the top of the separation column. We produced 1500 L of deuterium; each complete filling of the system requires about 700 L. Previous measurements demonstrated an increase of the protium concentration at a rate of 1 ppm per day. Since the critical concentration of protium for the experimental precision is at the level of 100 ppm, we changed the deuterium after 60 days of operation.

3.6 Purity Diagnostics

The capture rate of negative muons on nitrogen and oxygen nuclei is much larger than Λ_d, which means that the impurity level has to be reduced as far as possible, and the remaining impurities must be carefully measured. A purity requirement at the level of 1 ppb follows from the expected shift in the capture rate of approximately 2 s^{-1}/ppb for nitrogen and 1 s^{-1}/ppb for oxygen. In MuSun, the gas is cleaned by continuous circulation through zeolite absorbers in the CHUPS system, and we have developed a number of complementary techniques for the measurement. One of the highlights of R2013 was the demonstration of the consistency of these methods, which will be described in this section.

For the main production part of R2013, the TPC was operated at T=31 K, P=5.1 bar, corresponding to a density of ϕ=0.066 relative to LH_2 density. Most common impurities are expected to be cryopumped to the walls, except for N_2 and O_2. Because the CHUPS absorbers were saturated during the production phase, these impurities were present at concentrations dictated by their vapor pressure, 20 ppb for N_2 and 0.2 ppb for O_2 (see Figure 20). The origin of this saturation effect is not known, but it is suspected that the zeolite was accidentally exposed to air after it had been purged.

While this is in a way an unfortunate situation, it will provide an opportunity to demonstrate a zero-extrapolation procedure, as was used in the MuCap analysis, to correct for the high impurity concentration. In addition to the production runs, we also collected data with gas cleaned to a N_2 concentration of less than 1 ppb and doped to 1950 ppb (at a higher temperature of 37 K) and 525 ppb (at 34 K).

3.6.1 Gas Chromatography

A gas chromatograph is connected to the TPC through a 8 m stainless steel capillary sampling line. Impurities are enriched in an accumulating column in order to increase the sensitivity to the very small concentrations that are expected.

Significant checks of this gas chromatography system were performed during R2013. In the early part of the run, calibrations were performed by successive dilutions of a sample with pure deuterium and by repeated sampling from the TPC as it was cooled. Concentrations as low as 3 ppb of N_2 and 1 ppb of O_2 were detected successfully during these calibrations.

When the CHUPS absorbers were saturated, the result of the chromatographic analysis was 22±1 ppb N_2 at 31 K temperature, which agrees at the 10% level with other analysis methods. After the absorbers were purged, the measured concentration dropped below the threshold of detection of approximately 1 ppb. The subsequent doping of the gas provided an opportunity to make repeated measurements under the same conditions, which demonstrated good reproducibility.

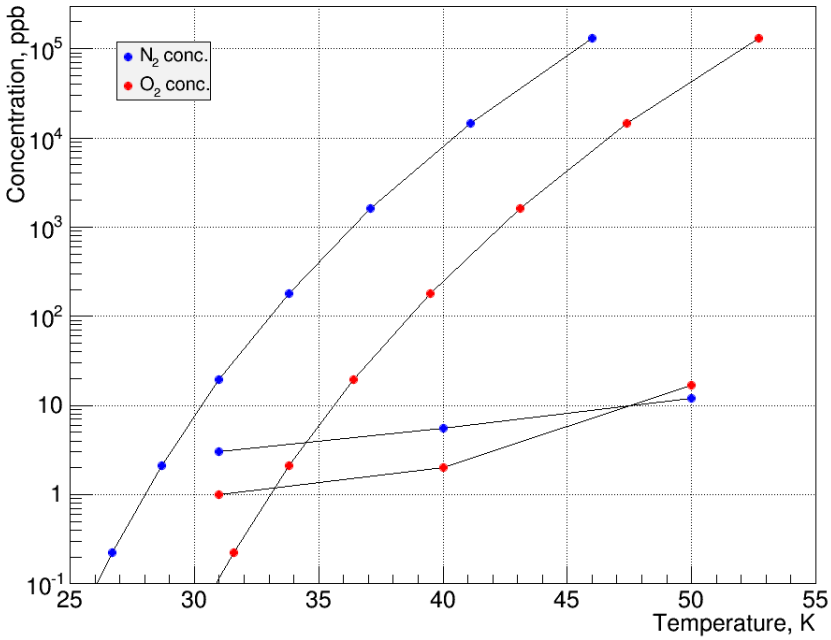

Figure 20: Upper curves: calculated equilibrium concentrations for N_2 and O_2 relative to MuSun gas density as function of temperature. Lower curves: concentrations measured by gas chromatography after purging CHUPS absorbers.

3.6.2 Direct Impurity Detection

The recoiling nucleus has an energy of order 100 keV, which yields a localized delayed signal of the muon stop in the TPC. It is a challenge to detect these rare events due to the large background from muon-catalyzed fusion products. This background can be partially suppressed by a delayed analysis cut, since the fusion yield from the μd quartet state, which is depopulated in a few μs, is two orders of magnitude larger than the doublet state rate. The background is further suppressed by setting the requirement that no Michel electron be present in the event, since a muon that has been captured cannot decay (see Figure 21). In addition, the significant improvement in energy resolution from the new preamplifiers further allows separation of the ^{3}He events from the capture recoils. This analysis method preliminarily gives a concentration of 19 ppb of N_2, in excellent agreement with the gas chromatography results. It was further tested with the cleaned and doped TPC conditions, again yielding consistent results.

In principle, an additional suppression factor is available: the capture is preceded by a transfer of the muon from the deuteron to the impurity, and an X-ray is produced in this transfer process. To detect these X-rays, we prepared an apparatus to hold a set of five thin NaI detectors (12.7 cm diameter, 1 cm thickness) as close as possible to the TPC vessel to maximize the solid angle coverage, replacing the standard electron detector during special runs. The X-ray tagging method is expected (based on Monte Carlo simulations) to suppress the ^{3}He peak relative to the capture events by a factor of $\sim$30. The frame also holds a set of plastic scintillators to veto events containing the Michel electron which would indicate that the muon was not captured. We assembled and tested this miniature X-ray/electron detector, preparing to deploy it at the end of R2013. Unfortunately, not enough beam time remained after the accelerator outage and other technical problems, so this study has been deferred to R2014.

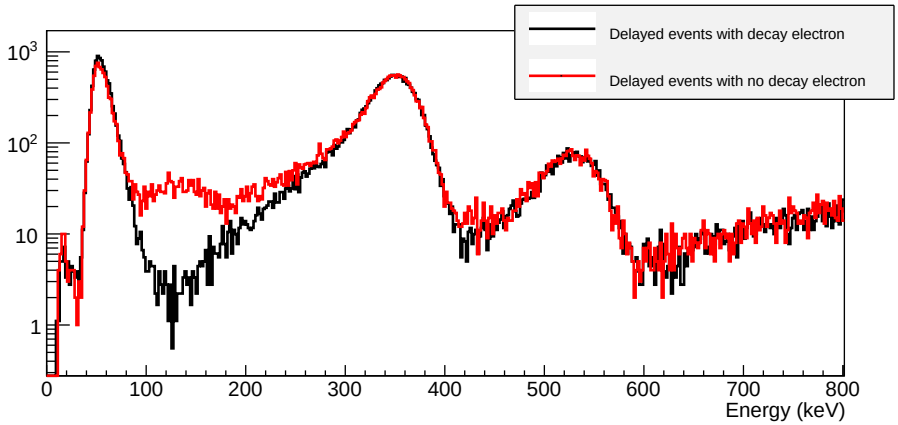

Figure 21: A cut on the detection of a Michel electron clearly separates the delayed energy spectrum in TPC in events with no captures and with captures on gas impurities. At the nominal conditions for the 2013 run, a clear capture signal is present at ∼125 keV.

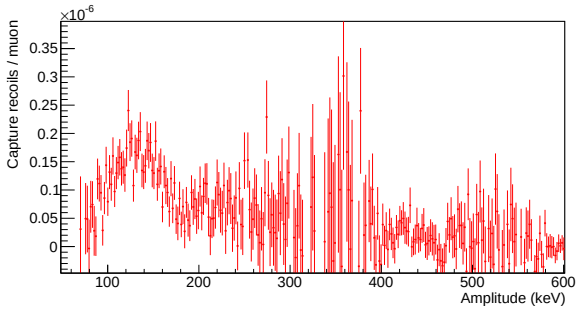

Figure 22: Impurity capture spectrum determined by subtracting the spectra shown in Figure 21.

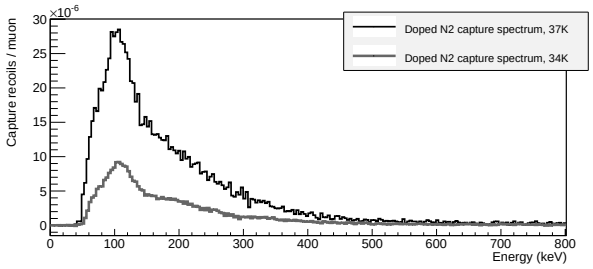

Figure 23: Recoil spectrum from muon capture on nitrogen with a N_2-doped D_2 target.

4 Plans and Beam Time Request 2014

4.1 Upgrade Plans

4.1.1 TPC

An outstanding problem after R2013 is the construction, testing and operation of a reliable TPC grid that meets the specifications outlined in Section 3.5.1. The concept is a composite frame, with the soldering and most mechanical structures being made of stainless steel. Only the distance bars in the wire direction will be made of tungsten, to eliminate sagging of the wires at cryogenic temperatures. A frame following this concept was made by the Morenzoni group at PSI and has been operating flawlessly for several years. The construction should allow the production of three or four frames, at reasonable cost and labor, so as to have spares. This implies keeping the tungsten components simple, as they are difficult to machine. A suitable layout suggests that the Macor posts of the field cage will now be mounted on the grid frame. At the same time, the machining of these posts will be simplified by using cylindrical rod structures. A new set of tungsten field wires will be prepared, with the thin entrance wires in the muon beam replaced by less brittle silver wires. All components will be manufactured at the University of Washington (UW), with the hard soldering of the stainless steel to tungsten to be done at the PSI workshop (the wires will be soldered by the PSI detector group). The preliminary CAD model of this design is depicted in Figure 24 and will be finalized before the PSI PAC meeting.

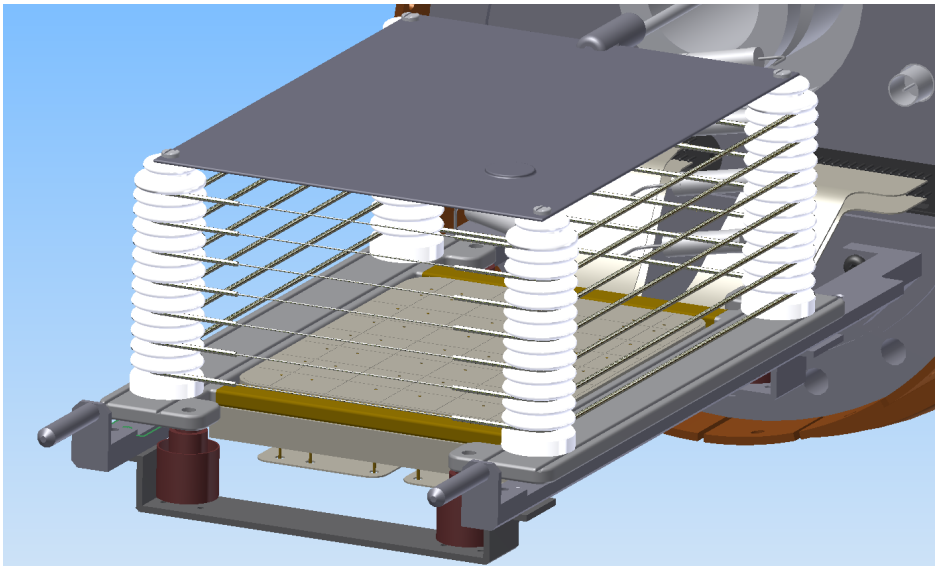

Figure 24: CAD model of TPC with composite grid frame.

4.1.2 Gas System

During the spring technical run we are planning to produce about 2000 L of isotopically pure deuterium. We will use a new coldhead for this operation in order to avoid disassembling the cooling system of the cryogenic TPC. We will also perform an isotopic analysis using the gas chromatograph of the deuterium from the end of R2013 and new deuterium for R2014. We will perform some routine maintenance of, for example, the nitrogen filling line, the CHUPS zeolites, and the Pt100 temperature probes, and we will modernize the readout system for the gas chromatograph.

4.1.3 Testing and Redundancy

The experience of R2013 emphasizes the importance of thorough testing and redundancy for an experiment of the complexity of MuSun. The collaboration will address this with the following plan. Three or four grid frames and two complete TPCs will be prepared. One TPC will be assembled at PSI during the planned April-May technical run of the PNPI group and fully instrumented with the help of the UW group. Ideally by mid-May, TPC1 should be operational, having been temperature-cycled; it will remain unchanged until the beginning of the main production run. In case of problems, improvements and further tests can still be scheduled. In parallel, the UW group has assembled a second TPC test stand based on less expensive LN_2 cooling in Seattle. This will be used to prepare an identical TPC2 in an independent pressure vessel. We already had such a set-up in place for R2013 to exchange TPCs without opening the target chamber. Unfortunately, this low-risk exchange failed due to a cold leak that was not detectable at room temperature, and we had to swap the pressure vessel as well. Thus, the first task of the UW group will be to locate this leak and prepare the second vessel while the new grid is being constructed. TPC2 will then undergo more extensive temperature cycling including several spare cryo-preamplifiers, to further systematically assess the resilience against hard-to-predict temperature effects. For the production run, both TPC setups should be closed and operational. An exchange would then be possible within a few days.

4.1.4 WFD Synchronization

One of the unfortunate features of the WFD data is a four clock tick ambiguity (4CTA). Although the origin of the ambiguity is obscured in the details of firmware design challenges dating back to 2003, the

symptoms are obvious enough. Depending on where the START signal arrives with respect to the phase of the external clock, the timing offset between different channels on different WFD boards can jump back and forth by 4 clock ticks, corresponding to 160 ns in the TPC WFDs. In the scintillator detectors of MuLan and MuCap, where the signals in different elements are independent, the 4CTA is relatively benign. However for the TPC WFDs, where signals in adjacent pads form tracks, the 4CTA degrades the resolution.

Eliminating the 4CTA requires changes to both hardware and firmware. We have built a simple VME module to provide a synchronized START: that is to say a START signal that is synchronous with the clock. We have written the firmware to enforce the synchronization of all WFDs in a crate, which can be invoked at begin run time. Preliminary results are promising but full implementation awaits further tests.

4.1.5 Kicker Stewardship

The kicker performed fairly well in R2013. A few MOSFET cards failed early on, but after they were replaced, there was no further trouble. All the same, the kicker remains a significant vulnerability for any production run. The main problem is that there are no kicker experts within the MuSun collaboration or at PSI. Routine technical maintenance of timing alignment and cleaning of the fiber optic trigger cards has not been performed for several years. A major problem, more serious than the death of a couple of MOSFET cards, could easily stop production for several days. We request that PSI take responsibility for the kicker as it would for any beamline element. The kicker would be made available for other experiments as well. The task would not be onerous. Someone from the PSI RF group should review the design, consulting with Mike Barnes (from the RF group at TRIUMF, now at CERN). The schematics should be updated; in the present 2-cabinet mode, we have sufficient MOSFET cards to see us through to the end of MuSun. However, any hard-to-get-parts should be identified and spares should be obtained. We should re-establish routine maintenance of the cabinets. Here, the MuSun collaboration can certainly help. To preserve our knowledge, we should make a detailed video of all the maintenance procedures.

4.2 Beam Request

In 2014 we request beam time for a major MuSun production run in πE1. The optimal time window would be three 4-week blocks from July 21 to October 13. An earlier start is not possible, because of the above mentioned upgrades and tests, including a sufficient safety margin. A later start would strongly reduce the participation of young students and, in particular, teaching faculty, whose expertise is required to set up the experiment. Experience has shown that requesting less than three months for the complex MuSun experiment is not efficient.

In preparation of the run we plan extended technical work at PSI in April and May and a start-up of all components two weeks in advance of the production run. The πE1.2 MuSun set-up area should be shielded from the πE1.1 section to allow free access during the MuSun area during normal beam production.

- 2 weeks: Commissioning all new elements. Set-up of the experiment for production with beam. Optimization of all parameters (beam, chambers) for highly efficient production.
- 9 weeks: Production to collect a statistics of about 10^{10} $\mu - e$ events, 70 % μ^- and 30 % μ^+. Here events refers to fully reconstructed pairs, which pass all final analysis cuts. This amounts to half of the statistics required for concluding MuSun.
- 1 week: Systematic measurements, including purity studies. This will include measuring capture yields with new NaI array to clean up the signals with an X-ray coincidence and verifying the monitoring sensitivity and background by temperature scans.

References

[1] MuSun Collaboration (http://muon.npl.washington.edu/exp/MuSun):
V.A. Andreev, E.J. Barnes, R.M. Carey, V.A. Ganzha, A. Gardestig, T. Gorringe, F.E. Gray, D.W. Hertzog, M. Hildebrandt, L. Ibanez, P. Kammel, B. Kiburg, S.A. Kizilgul, S. Knaack, P.A. Kravtsov, A.G. Krivshich, K. Kubodera, B. Lauss, M. Levchenko, X. Luo, K.R. Lynch, E.M. Maev, O.E. Maev, F. Mulhauser, M.H. Murray, F. Myhrer, K. Neely, A. Nadtochy, C. Petitjean, G.E. Petrov, J. Phillips, R. Prieels, D. Prindle, N. Raha, R. Ryan, G.N. Schapkin, N. Schroeder, G.G. Semenchuk, M.A. Soroka, V. Tishchenko, A.A. Vasilyev, A.A. Vorobyov, N. Voropaev, M.E. Vznuzdaev, F. Wauters, P. Winter.

[2] Andreev, V. et al. *Phys. Rev. Lett.* **110**, 012504 (2013).

[3] Chen, J.-W., Inoue, T., Ji, X.-d., and Li, Y.-C. *Phys. Rev. C* **72**, 061001 (2005).

[4] Kammel, P. and Kubodera, K. *Annu. Rev. Nucl. Part. Sci.* **60**, 32753 (2010).

[5] Tishchenko, V. et al. *Phys.Rev.* **D87**(5), 052003 (2013).

[6] Bunemann, O., Cranshaw, T. E., and Harvey, J. A. *Can. J. Res.* **A 27**, 191 (1949).